Ultramicroscopy 262 (2024) 113978

Contents lists available at ScienceDirect

Ultramicroscopy

journal homepage: www.elsevier.com/locate/ultramic

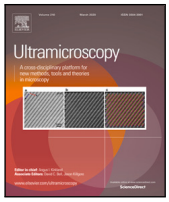

Influence of magnetic field on electron beam-induced Coulomb explosion of gold microparticles in transmission electron microscopy

Wen Feng [a,*], Thomas Gemming [a], Lars Giebeler [a], Jiang Qu [a], Kristina Weinel [b], Leonardo Agudo Jácome [b], Bernd Büchner [a], Ignacio Gonzalez-Martinez [a]

[a] Leibniz Institute for Solid State and Materials Research (IFW) Dresden, Helmholtzstr.20, Dresden, 01069, Germany
[b] Federal Institute for Materials Research and Testing (BAM), Unter den Eichen 87, Berlin, 12205, Germany

ARTICLE INFO

Keywords:
Electron beam-induced fragmentation
Coulomb explosion
X-ray diffraction
Lorenz transmission electron microscopy
Electron beam-induced charging

ABSTRACT

In this work we instigated the fragmentation of Au microparticles supported on a thin amorphous carbon film by irradiating them with a gradually convergent electron beam inside the Transmission Electron Microscope. This phenomenon has been generically labeled as "electron beam-induced fragmentation" or EBIF and its physical origin remains contested. On the one hand, EBIF has been primarily characterized as a consequence of beam-induced heating. On the other, EBIF has been attributed to beam-induced charging eventually leading to Coulomb explosion. To test the feasibility of the charging framework for EBIF, we instigated the fragmentation of Au particles under two different experimental conditions. First, with the magnetic objective lens of the microscope operating at full capacity, i.e. background magnetic field $B = 2$ T, and with the magnetic objective lens switched off (Lorenz mode), i.e. $B = 0$ T. We observe that the presence or absence of the magnetic field noticeably affects the critical current density at which EBIF occurs. This strongly suggests that magnetic field effects play a crucial role in instigating EBIF on the microparticles. The dependence of the value of the critical current density on the absence or presence of an ambient magnetic field cannot be accounted for by the beam-induced heating model. Consequently, this work presents robust experimental evidence suggesting that Coulomb explosion driven by electrostatic charging is the root cause of EBIF.

1. Introduction

As a powerful and indispensable approach for nanomaterials characterization and nanoengineering, transmission electron microscopy (TEM) occupies a central place in various fields ranging from materials science, chemistry to physics and nanotechnology. However, the TEM has outgrown its role as a device almost exclusively devoted to characterization. It increasingly becomes a platform for in-situ nanoengineering as well as a microlaboratory for studying dynamic processes in real-time with unparalleled visual resolution, i.e. realized by special TEM specimen holders for heating or cooling and even with STM tips, flow cells or the option to inject gas to a certain sample position. [1–3] However, it is also possible to produce nanostructures in all three dimensionalities without the need of custom holders or expensive modifications to the TEM itself. [4–6] Our work is an example of the latter, showcasing a synthesis method that relies solely on a simple irradiation protocol, the "convergent beam protocol" or CBP. Implementing simple synthesis methods inside the TEM provides advantages seldom available by other means, namely, it makes it possible to directly peer into crucial aspects of the formation mechanisms. Additionally, a large array of characterization methods are used at the experimenter's disposal to study the pristinely produced nanostructures (e.g. energy- dispersive X-ray spectroscopy (EDS), electron energy loss spectroscopy (EELS), electron diffraction (ED), high-angle annular dark-field imaging (HAADF)).

The e-beam-driven synthesis protocols implemented in the TEM turn some of the various radiation damage mechanisms (they typically pose a challenge to high resolution electron microscopy) to the experimenter's advantage [7,8]. An example of this is a generic phenomenon known as "electron beam-induced fragmentation" (EBIF) which can be described as the deposition of large numbers of nanoparticles suddenly produced by material expelled from a single microparticle precursor subjected to e-beam irradiation.

The physical roots of EBIF have been a topic of debate since the phenomenon was first observed in 1997. [9] Ever since then, the scientific community has split into two main "camps" that support physically distinct explanations of the phenomenon. On the one hand, there is a group proposing a theory based on beam-induced heating or e-beam evaporation to explain EBIF [10–16], and on the other,

* Corresponding author.
E-mail addresses: w.feng@ifw-dresden.de (W. Feng), martinezignacio.gonzalez@infineon.com (I. Gonzalez-Martinez).

https://doi.org/10.1016/j.ultramic.2024.113978
Received 22 November 2023; Received in revised form 21 February 2024; Accepted 20 April 2024
Available online 22 April 2024

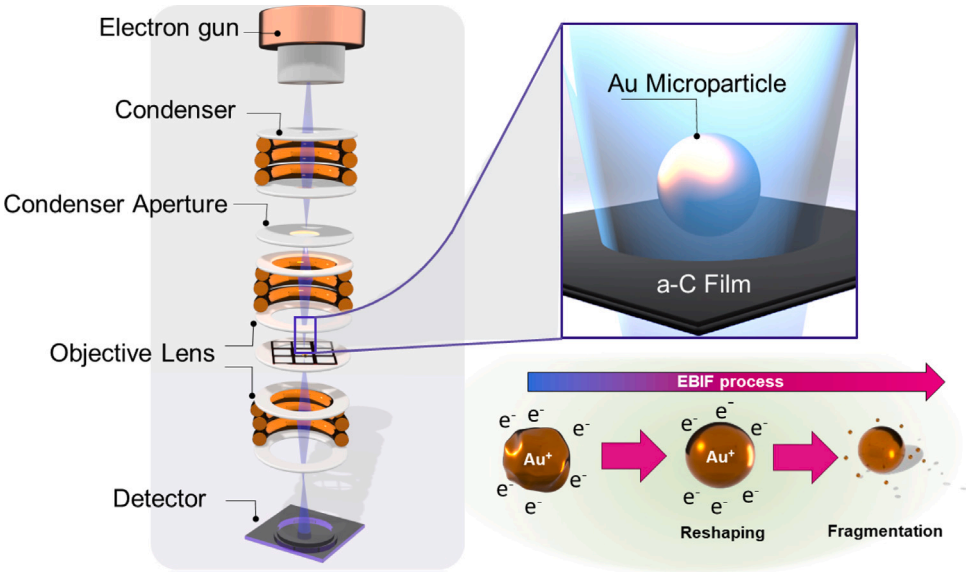

Fig. 1. Schematic illustrations of a TEM column demonstrating the principle of electron beam induced fragmentation process. Inset micrograph shows irradiated Au microparticle in the specimen plane.

there is a group that favors an explanation based on beam-induced charging [5,17–25] which sometimes has been explicitly identified as a manifestation of "Coulomb explosion". Furthermore, variations of the charging-based hypothesis have been made to explain phenomena in which the irradiated precursor microparticles do not fragment, but instead produce nanowires that gradually protrude for the time of irradiation. [21,26,27] What advocates of both paradigms have in common, is that the evidence they have advanced is largely speculative and/or theoretical. It is therefore in need of conclusive experimental support.

In this work, we focus on studying how the presence and/or absence of a magnetic field affects the EBIF of Au microparticles (MPs) supported on a thin amorphous carbon (a-C) film. To realize this experiment, groups of Au microparticles were subjected to two different experimental conditions. In one group, EBIF was instigated in the presence of a 2 T magnetic field generated by the objective lens of the TEM acting at its full capacity. For the second group the objective lens was switched off (Lorenz mode) thus eliminating the ambient magnetic field ($B = 0$ T) wrapping the specimen. The sketch of a TEM column demonstrates the principle of EBIF in Fig. 1. Our findings show that the presence or absence of the magnetic field significantly alters the critical current density at which the particles fragment. This finding favors the theoretical paradigm that identifies EBIF as a charging-driven phenomenon. Based on the kinetics of this charged-induced phenomenon, it is understandable why some authors have described it as an instance of Coulomb explosion. However, the significantly smaller scale of the systems are typically responsible for a Coulomb explosion (nanoparticles rather than microparticles) without leaving "parent" microparticles as precursor, calling it "Coulomb peeling" might be more appropriate.

We present a theoretical framework which explains the difference in critical current densities, with and without the presence of the magnetic field affecting the transport of current along the a-C film substrate. This framework is supported by Raman, X-ray diffraction (XRD), selected area electron diffraction studies (SAED) of the a-C films and the resistance measurements of the Au/a-C contact.

2. Experimental methods

We deposited Au microparticles (1.5 ∼ 3.0 μm spherical powder, 99.96% purity, Goodfellow) onto the amorphous carbon (a-C) film of a commercial TEM grid (Copper/C film, 200 mesh, Type S 160,

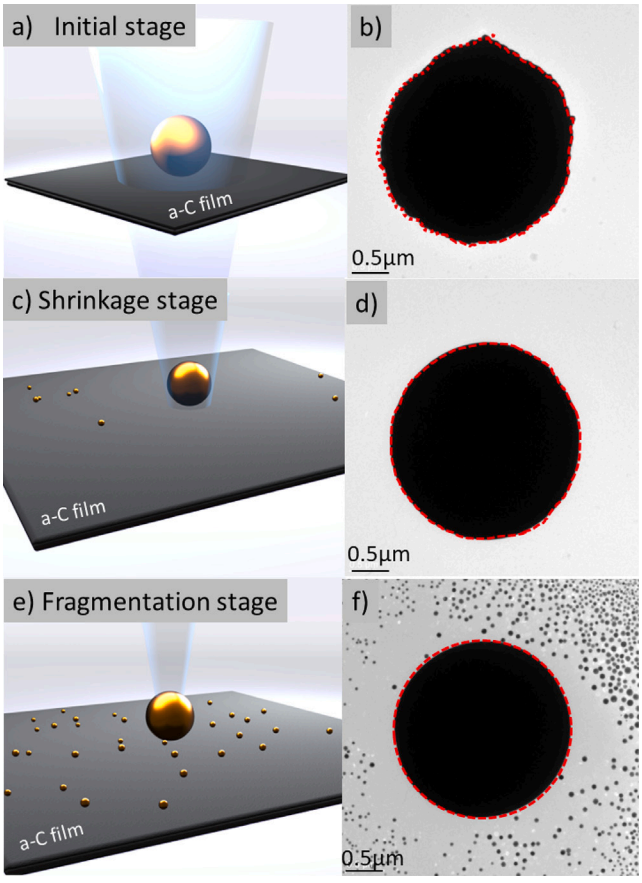

Fig. 2. Schematic illustrations of stepwise convergent irradiation protocol are shown in (a), (c) and (e) which summarize the whole process from initial, shrinkage and fragmentation stages, respectively. The current density at the shrinkage stage (J_S) is 1018.0 A/cm^2 and 1450.6 A/cm^2 at the fragmentation stage (J_F) which are presented in (d) and (f), respectively. The current density at the initial stage in (b) is below 50 A/cm^2.

Plano) by direct dry transfer. Electron beam-induced fragmentation was carried out at 300 kV in a Thermo Fisher Titan 80–300 with third-order spherical aberration correction. We irradiated the particles under two irradiation conditions: first, in standard bright field (BF) mode with the objective lens operating at full capacity, i.e. $B = 2$ T; and in BF Lorenz mode, with the objective lens switched off, i.e. $B = 0$ T. In all EBIF experiments, the particles were irradiated by a gradually convergent e-beam protocol. That is, reducing the e-beam diameter via re-configurable condenser lens 2 (CL2) to trigger the modification of the current density, albeit that the magnitude of the primary current I_P barely changes (nearly 40 nA) in both conditions to keep the electron energy comparable. At sufficiently low current densities (< 50 A/cm^2) the particles remain stable. As the beam converges upon them and the current density increases, the particles begin to visibly shrink (shrinkage stage) and eventually undergo an "explosive" reaction (fragmentation stage) hereafter they expel multiple nanoparticles that become deposited on the surrounding a-C substrate. A schematic drawing of the CBP and the evolution of the microparticles are displayed in Fig. 2. All EBIF experiments were recorded in order to determine the current density irradiating the microparticles "frame by frame". (see supporting Movies 1 and 2 in the supplementary material section 3 for details)

The structure of obtained samples was characterized by the X-ray diffraction using a STOE Stadi P diffractometer with a curved Ge (111) primary beam monochromator and a Mythen 1 K detector (Dectris) was used. To fix the grid in the sample holder, a holey paper mask was adapted to the grid size but gently smaller in diameter. The grid is fixed with the paper mask and locked with a 3 mm-metallic mask and both were placed into the transmission sample holder without the usual acetate foil. The measurements were performed in transmission geometry at continuous spinning with only the paper mask, on the paper mask with an empty grid without gold and the gold-deposited grid with Cu $K\alpha_1$ radiation ($\lambda = 1.5406$ Å). As the range 2 ~ 60° 2θ was selected with a step size of 0.5° 2θ and 275 s measurement time per step to resolve the very weak signals of the components of interest.

3. Results and discussion

TEM micrographs representative for each stage of the EBIF process are shown in Figs. 2 (b), (d) and (f) accompanied by schematic pictures of each step (Figs. 2 (a), (c) and (d), respectively). Initially, the Au microparticle is stable as long as the irradiating current density is below a critical threshold value $J_S = 50$ A/cm^2 (Fig. 2 (a)). As the beam gradually converges and the current density approaches the critical value ($J_S = 500$ A/cm^2 at $B = 2\ T$ and $J_S = 60$ A/cm^2 at $B = 0$ T), the particle "rounds up", i.e. the jagged outlines of their surface become significantly smoother (Fig. 2 (d)). Careful observations of the recordings of the process as well as measurements of the projected cross sections of the MPs, point to a first loss small amounts of material which marks this point as the beginning of the ablation process and therewith of the "shrinking stage", in other words, once J_S is reached, the particle begins to shrink (Figs. 2 (c) and (d)). With on-going beam convergence, the particle fragments at the outermost layers and form nanoparticles which are deposited on the a–C substrate (Figs. 2 (e) and (f)). We refer this phenomenon to a "critical current density" to the value J_F at which fragmentation occurs.

We observed that both J_S and J_F are affected by the presence or absence of the magnetic field. When $B = 0$ T, nearly 93.8% of the particles began to shrink at a current density of < 500 A/cm^2 (red dash line in Fig. 3 (a)). On the other hand, 98.2% of the particles irradiated at an ambient field of $B = 2\ T$ entered the shrinkage stage above a current density of 500 A/cm^2. This phenomenon is observed in Fig. 3 (a) where J_S is plotted as a function of the initial particle's radius. In fact, some MPs irradiated at $B = 2\ T$ (33%) began to shrink at current densities of around 2000 A/cm^2 or higher, i.e. at least 4 times larger than the value at which 96.9% of the MPs irradiated at $B = 0\ T$ enter the shrinkage stage (500 A/cm^2). The distribution of Au MPs as a function of current density threshold J_S and J_F at $B = 0\ T$ (Lorenz mode) and $B = 2\ T$ are shown in Figure S2 and S3 of the supplementary material section 4, respectively.

As a way to account for errors or imprecisions in our method for determining punctual J_F values, we also recorded the values of the current densities one second before the determined J_F values plotted in Fig. 3 (b). With the exception of a single MP irradiated at $B = 2$ T, every other MP underwent fragmentation at $J_F > 1000$ A/cm^2. In contrast, all the particles irradiated at $B = 0\ T$ began to fragment at $J_F < 500$ A/cm^2. In other words, the critical current density J_F at 2 T is more than twice as large than its counterpart at 0 T.

There are two reasons why the number of MPs in the J_S plot is larger than that in the J_F plot. Firstly, not every shrinking particle fragments with increasing current density. Secondly, when the MP diameter exceeds the diameter of the beam probe necessary to reach J_F, then the determination of the moment at which fragmentation occurs fails from the clips recorded of the process. In summary, the results show that there is a measurable difference between J_S and J_F when the CBP is implemented on the Au MPs at $B = 2\ T$ compared to those irradiated in the absence of a magnetic field.

To get information on the crystallinity of the components and the content, X-ray powder diffraction patterns were measured. In Fig. 4 (a) the X-ray diffraction patterns are displayed for the paper mask-only measurement, the paper mask with a fresh, unused copper grid of the type G2720C (Agar Scientific), as well as two a-C film samples Q10 and O10 in the range of 10° ≤ 2θ ≤ 60°. Fig. 4 (b) shows an enlarged view of the range 10° ≤ 2θ ≤ 30° with partial curves of the some diffraction patterns to clearly illustrate the presence additional reflections for sample O10 which are absent in all other measurements. To accentuate the low intensity reflections of possible carbon contents, the intensity is shown in a logarithmic scale.

The reflections of face-centered cubic Cu [28] from the TEM grid and mainly rhombohedral $CaCO_3$ used as a common paper filler [29,30] are in evidence. Two reflections of possible carbonaceous phases are visible at about 16.5° and 22.5° 2θ. Carbon #1 (marked in Fig. 4 b) shows a very broad reflection with a FWHM of about 3° 2θ which helps to estimate the crystallite size to max. 2 nm by a simple calculation with the Scherrer formula. The crystallite size for carbon #2 (marked in Fig. 4 b) was estimated to about 4 nm with the same procedure and with a FWHM of 1.3° 2θ. From the very weak intensities of the two strongest reflections, all weaker reflections are below the detection limit, and therefore only a small trace of carbon is expected.

The hexagonal graphite structure type with the space group P63/mmc was used to index both reflections with the Miller indices 002. In literature, lattice shrinking is usually discussed with a reduction of defects, e.g. as induced by a heat treatment [31,32]. As both reflections are separated by 6° 2θ from maximum to maximum, a lower degree of crystallinity and a higher amount of defects is probable for carbon #1 compared to carbon #2. This interpretation is supported by the FWHM of carbon #1 which is more than twice as large as that of carbon #2. Both described observations agree with literature [31,32]. According to the given previous observations and interpretations, the diffraction pattern of the a-C verifies that the formed a-C thin film is a mixture of amorphous carbon and randomly oriented nanoclusters. This information conveyed by the diffraction pattern correlates well with the Raman results (see Raman spectra and SAED of a-carbon thin film in the supplementary material section 1: Figure S1).

As mentioned in the introduction, there are two traditional paradigms that attempt to explain the physical basis of EBIF, namely, beam-induced heating [10–16] and beam-induced charging or Coulomb explosion [5,18–24]. If EBIF is dominantly a consequence of the microparticles absorbing and transforming a fraction of the primary beam's energy into heat, then it becomes difficult to determine the physical mechanisms by which the magnetic field could influence the heat generation so dramatically. On the other hand, if EBIF is a phenomenon

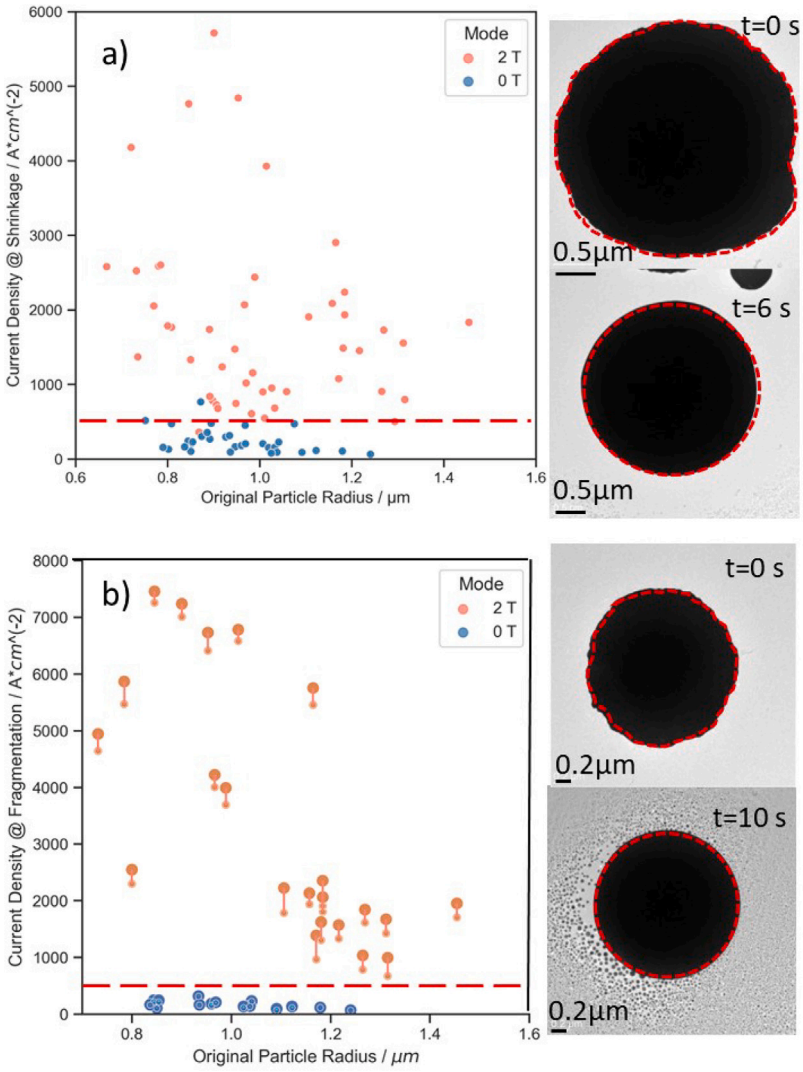

Fig. 3. Critical shrinkage current density J_S and critical fragmentation current density J_F as a function of the particle's radius in (a) and (b) respectively. The red and blue points represent current density at $B = 2\ T$ and $B = 0\ T$ (Lorenz mode) respectively. The red dashed line represents the current density of 500 A/cm^2. The error bars in (b) represent the current densities at one second before fragmentation stage. The blue dots have error bars but that they are much smaller in comparison.

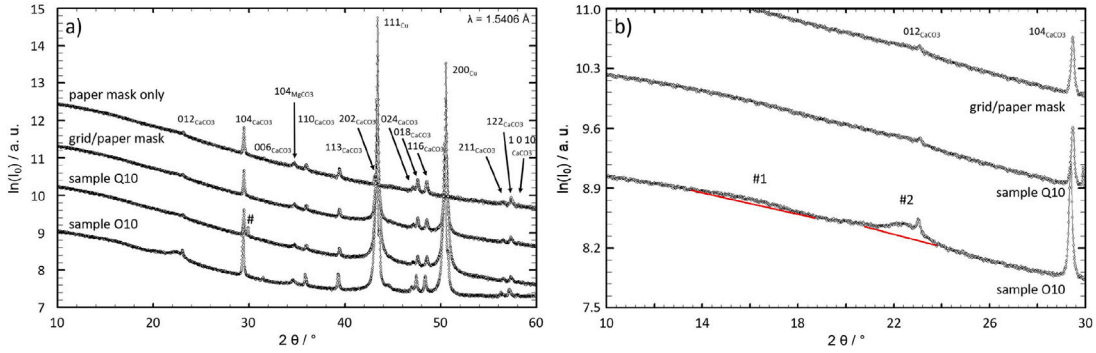

Fig. 4. (a) X-ray diffraction patterns using Cu $K_{\alpha 1}$ radiation (λ = 1.5406 Å) of amorphous carbon films deposited on Cu grids. As references the patterns from the paper mask and with or without a fresh, unused copper grid are represented in the two upper curves respectively. Two different amorphous carbon films "O10" and "Q10" are given as the two lower lines with the sample O10 as the lowest. (b) Enlarged view of the range of 10 - 30° 2θ with the two marked reflections as possible carbon contributions.

notably based on the accumulation of charge in the precursor microparticles, then there is a clear theoretical basis to explain how charging can be affected by switching the magnetic field on and off. To understand how a charging-based mechanism is compatible with the observed results we need to consider the charge-balance equation of that calculates the rate of charging of the Au MP suspended over the a-C film [33]:

$$\frac{dQ}{dt} = I_{SE} + I_T - I_P - I_S \tag{1}$$

The charge contained within the particle at any given time is denoted by Q, and dQ/dt represents the change in Q over the duration of irradiation t. The current of secondary electrons (SEs) generated by the primary beam that exit the particle is I_{SE}. I_P represents the current of primary electrons impinging upon the particle, and I_T is the portion of I_P transmitted through the particle. The current of electrons flowing from the support into the particle is denoted by I_S.

The range of 300 kV electrons through gold is estimated to be R=84.9 μm using the "Stopping Power and Range Tables for Electrons" (ESTAR) [34]. Therefore it is reasonable to assume that most incoming electrons traverse the Au MPs which have diameters comparable with 1 μm. This means that $I_P \approx I_T$ and Eq. (1) becomes:

$$\frac{dQ}{dt} = I_{SE} - I_S \tag{2}$$

From Eq. (2) we can see that the net accumulated charge in the irradiated Au MPs is positive, since the magnitude of I_S is adjusted in response to the net emissions I_{SE}.

The term I_{SE} in Eq. (2) depends on the irradiated material, its size and the primary beam's energy [33]. It is described as:

$$I_{SE} = \delta \cdot J_{th} \cdot S \tag{3}$$

where δ denotes secondary electron yield which is a ratio between secondary electrons and primary electrons. S is the effective area of the Au MP. The value of δ equals 2.09 in the Au MPs under the condition of averaged current density threshold J_{th}= 1700 A/cm^2 based on energy retardation power formula [35–37]. This value also reveals the Au MPs is positive after e-beam irradiation.

The term I_S in Eq. (2) is the electronic current responsible for mitigating the positive charge accumulation in the irradiated Au MP. The current of electrons I_S from the substrate flowing into the particle across such a contact can be estimated by [38]:

$$I_S = A \cdot e^{q\cdot(V-\Phi_B-I_S R_T)/(k_B T)} \tag{4}$$

where A is the modified Richardson constant, q is the elementary charge, Φ_B is the barrier height between a-C substrate and Au MP, V is the potential of Au MP, T is the room temperature, k_B is the Boltzmann's constant. We assume R_T represents all resistive contributions coming from substrate electrons which transport along the substrate and the resistance at the Au/a-C interface.

The positive charge $Q(t)$ exerts a driving force on the electrons that constitute the current I_S, causing them to flow to the Au particle. The higher magnitude of I_S implies a higher critical current density J_F, because I_S escalates, it assists the efficiency in mitigating superficial charging, consequently restraining the fragmentation process induced by the uncontrolled proliferation of positive charges on the particle's surface.

Substitute Eq. (4) and Eq. (3) into Eq. (2), the accumulation of charge of Au MP as the function of irradiation time was obtained, as shown in Fig. 5. The time for the saturation process takes only 0.75 ns when the current density reaches to 1700 A/cm^2.

Coulomb explosion occurs when the net accumulated positive charge surpasses the "critical charge" that the Au MPs are able to withstand before their outermost atomic layers get expelled due to the repulsive forces building up between superficial Au ionized nuclei. According to

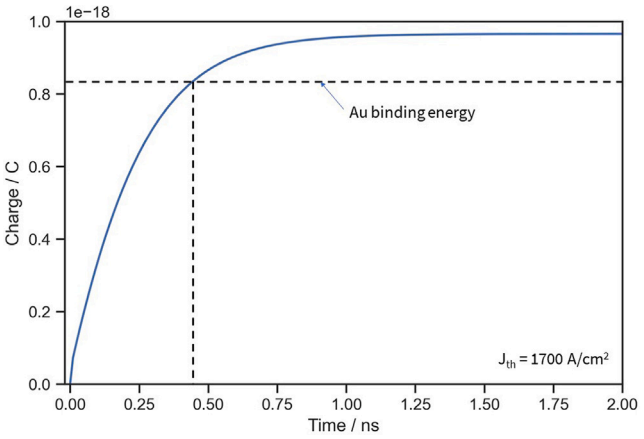

Fig. 5. Accumulation of charge $Q(t)$ as the function of the irradiation time in the condition of the current density J_{th} = 1700 A/cm^2.

the definition of Coulomb's Law, the Coulombic force can be derived as:

$$F = E \cdot Q(t) \tag{5}$$

where E denotes electric field, which equals $\frac{Q(t)}{8\cdot\pi\cdot\varepsilon_0\cdot r^2}$, the radius for Au labeled as r is 0.5 μm. The interlayer distance for Au labeled as d is 0.25 nm. Theoretically the Coulombic force is strong enough to overcome the Au atomic binding energy E_0 (80 eV for Au), which would be induced in the case of $F \cdot d > E_0$, Au MPs undergo the explosive reaction. Thus the threshold time for Coulomb explosion of Au MP only takes 0.43 ns in the condition of the current density J_{th} = 1700 A/cm^2 (Fig. 5).

a-C films has been observed to present a negative magnetoresistance; this finding is supported by the Grain Boundary Scattering theory (GBS) [39–41]. Although the magnetoresistance reported in the literature gives rise to only approximate 2% elevation of conductivity for our experimental conditions. However, harnessing the merit including the magnetic field assisted tunneling emission across the van der Waals (vdW) metallic contacts [42–45], a non-linear increase in the current of electrons flowing from a-C into the Au MPs can be efficiently realized with the presence of magnetic field. (Figure S6 in supplementary material section 8 interprets this mechanism as a schematic diagram.)

The negative magnetoresistance of Au/a-C contact has been further confirmed using Hall Effect Analyzer. The 4-probe measurements of the conductivity, resistance and Hall coefficient on the gold wire-bonded a-C film using the Hall Effect Measurement System with a 12.5 x 12.5 mm sensor (HCS 1– Hall Effect Measurement System, Linseis Messgeraete GmbH) were implemented which are depicted in Fig. 6. The IR curve of the Au/a-C contact at B = 0 T was acquired at room temperature with current swept from 5 to 45 nA. Fig. 6 (a) showcases the resistance drops with the increase of supply current indicating the semiconducting electrical transport property in the Au/a-C junction. After switching the magnetic field B to 1 T at$t$ = 20 s, the resistances of the Au/a-C contact overwhelmingly reduced from 68 to 35 kΩ averaged by values at 13 different measuring points on the specimen (Fig. 6 (b). All these findings added more puzzles to understanding the influence of the magnetic field on the current density-dependent damage.

Consistent with the proposed working principle, the Hall Effect measurements of Au/a-C contact show obvious negative magnetoresistive behaviors. Therefore, I_S at $B = 2\ T$ is higher than that at $B = 0$ T. This result is also consistent with our experimental conclusions. On the one hand, when the field is on, the transport of the electrons from the substrate into the Au particles is facilitated due to lower R_T, which helps to mitigate the positive charging growing on the particle surface, since, when the field is absent the negative magnetoresistance effect

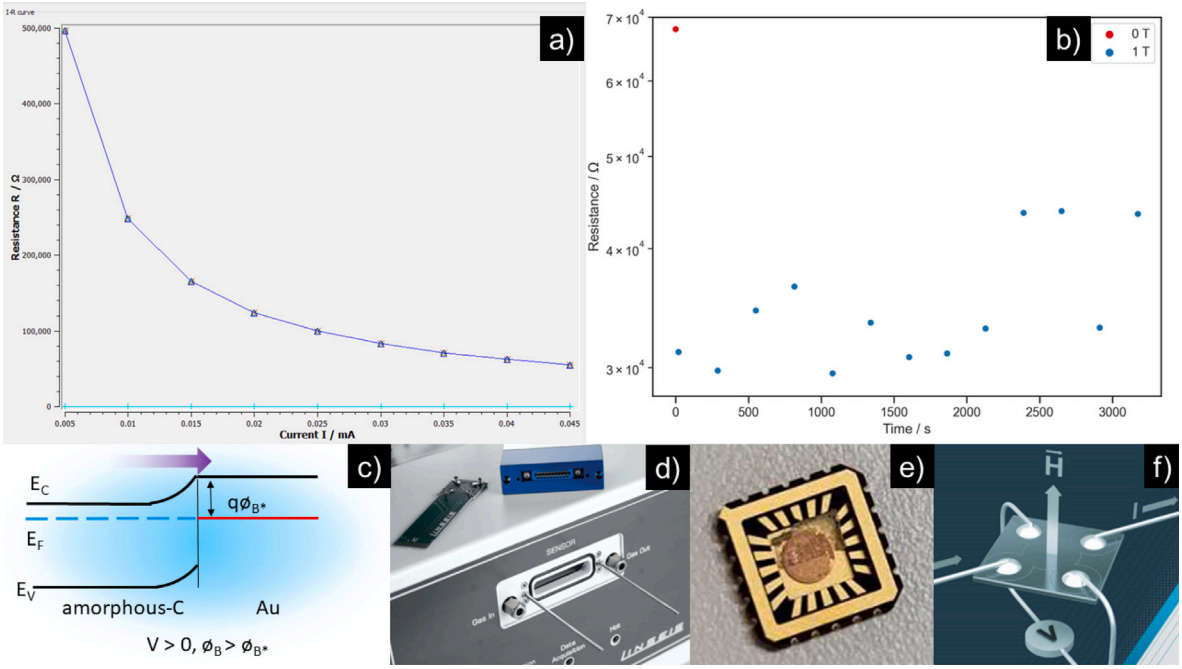

Fig. 6. Magnetoresistance Measurement of Au/a-C contact. (a) Pristine IR curve with B = 0 T and supply current swept from 5 to 45 nA. (b) Consecutive resistance measurements established at 13 different points on the a-C specimen at B switched from 0 to 1 T denoted as red and blue dots, respectively. (c) The band diagram applying forward bias where the barrier height before and after employing forward bias are denoted as $q\phi_B$ and $q\phi_B*$, respectively. The purple arrow indicates the electron transport direction. E_C, E_F and E_V: conduction band energy, Fermi level and valence band energy, respectively. (d) and (f) Schematic illustration of the Hall Effect Measurement System and working principle. (Images from Linseis Messgeraete GmbH) (e) Home-made gold wire-bonded a-C TEM film with underlying copper grid.

plays no role in promoting the transport of electrons from the a-C substrate into the Au particles. This statement means that the runaway accumulation of superficial charges on the Au microparticles can be triggered at lower critical current densities J_F since it is harder for the substrate electrons to flow into the particles to re-establish an electrostatic equilibrium.

Moreover, long-exposed Au MPs under extreme electron irradiation were observed up to 180 s. (See supplementary material section 7) The sizes of Au MPs were retained at micro-scale and extraordinarily stable after fragmentation. The expelled Au nanoparticles (NPs) were dispersed asymmetrically on the surface of substrate. This indicates that the substrate is uniformly charged and the Au NPs/a-C contacts are perfect [17]. We speculate that formation of NP-free stripes is associated with the interaction between charged NPs and substrate, driven by the inhomogeneous distribution of electric potential.

It has been inferred that when the crystalline dimension decreases below 10 nm, the scattering at crystal boundaries becomes one of the predominant factors that restricts the charge carrier mean free path [46]. From Raman analysis in the supplementary material section 1: Figure S1 we found the sp^2 domain size close to this range. Therefore the negative magnetoresistance of a-C films based on the GBS theory is applicable to our case.

At last, the timescale based on heating mechanism which is calculated in the supplementary material section 5 is much longer than that supported by electrostatic charge driven mechanism. This also certifies that EBIF should be dominantly the consequence of Coulomb explosion.

4. Conclusions

The role of the magnetic field mechanism as inferred from the field-dependent variation of the critical current density to initiate the fragmentation of the Au particles strongly indicates that the fragmentation phenomenon is electrostatically driven instead of thermally triggered. Theoretical simulations unveil Coulomb explosion is in picosecond scale (i.e. 430 ps) when the current density threshold reaches the certain critical value of 1700 A/cm^2 for the Au MPs. If the EBIF is attributed to heating, all Au MPs should be totally lost in the form of evaporation in microsecond scale (i.e. 7.5 μs) but not reaching to a steady state which are observed in our experiments. Furthermore, the magnetic field effect seems to facilitate the transport of electrons from the a-C substrate into the Au particles, which is consistent with current knowledge about the electrical properties of a-C films [39]. This leads us to conclude that beam-induced fragmentation is a phenomenon that should be conceptualized as an instance of Coulomb explosion.

CRediT authorship contribution statement

Wen Feng: Writing – original draft, Validation, Software, Investigation, Funding acquisition, Formal analysis. **Thomas Gemming:** Project administration. **Lars Giebeler:** Formal analysis, Validation. **Jiang Qu:** Formal analysis, Validation. **Kristina Weinel:** Writing – review & editing. **Leonardo Agudo Jácome:** Writing – review & editing. **Bernd Büchner:** Supervision. **Ignacio Gonzalez-Martinez:** Conceptualization, Investigation, Formal analysis.

Declaration of competing interest

The authors declare the following financial interests/personal relationships which may be considered as potential competing interests: Wen Feng reports financial support was provided by Leibniz Institute for Solid State and Materials Research Dresden. Kristina Weinel reports financial support was provided by BAM Federal Institute for Materials Research and Testing. If there are other authors, they declare that they have no known competing financial interests or personal relationships that could have appeared to influence the work reported in this paper.

Data availability

Data will be made available on request.

Acknowledgments

W.F. and K.W. thank IFW and BAM for financing IFW-BAM tandem program. W.F. thanks Jiang Qu, Antonius Dimas Chandra Permana and Lars Giebeler for the assistance with the implementation of Raman and XRD measurements, respectively. We further thank Sandra Nestler and Jun Yang for the assistance with wire bonding and Hall Effect measurement, respectively. A special thank goes to Shengqiang Zhou, Yu Zhen and Ciaran Fowley from Helmholtz-Zentrum Dresden-Rossendorf (HZDR) for magnetoresistance measurements. This work was supported by the Leibniz Institute for Solid State and Materials Research (IFW) and Federal Institute for Materials Research and Testing (BAM), Germany.

Appendix A. Supplementary data

- Supplementary material on specimen preparation and Raman, SAED, X-ray diffraction of a-C film, distribution of Au microparticles as a function of current density threshold, electrical transport characterizations of gold wire-bonded a-C film and corresponding raw data retrieved from the software integrated in the Hall Effect Measurement operating system as well as details about the calculation of the timescale based on the heating mechanism (PDF)
- Movie 1: Au MPs fragmentation at current density J_F = 2341.7 A/cm^2 instigated by irradiation of gradually convergent electron beam (MP4)
- Movie 2: Au MPs fragmentation at current density J_F = 2089.6 A/cm^2 instigated by irradiation of gradually convergent electron beam (MP4)

Supplementary material related to this article can be found online at https://doi.org/10.1016/j.ultramic.2024.113978.

References

[1] J.Y. Cheong, J.H. Chang, H.K. Seo, J.M. Yuk, J.W. Shin, J.Y. Lee, I.-D. Kim, Growth dynamics of solid electrolyte interphase layer on SnO2 nanotubes realized by graphene liquid cell electron microscopy, Nano Energy 25 (2016) 154–160.
[2] M. Gu, L.R. Parent, B.L. Mehdi, R.R. Unocic, M.T. McDowell, R.L. Sacci, W. Xu, J.G. Connell, P. Xu, P. Abellan, X. Chen, Y. Zhang, D.E. Perea, J.E. Evans, L.J. Lauhon, J.-G. Zhang, J. Liu, N.D. Browning, Y. Cui, I. Arslan, C.-M. Wang, Demonstration of an electrochemical liquid cell for operando transmission electron microscopy observation of the lithiation/delithiation behavior of Si nanowire battery anodes, Nano Lett. 13 (12) (2013) 6106–6112.
[3] R.R. Unocic, K.L. Jungjohann, B.L. Mehdi, N.D. Browning, C. Wang, In situ electrochemical scanning/transmission electron microscopy of electrode–electrolyte interfaces, MRS Bull. 45 (9) (2020) 738–745.
[4] I. Gonzalez-Martinez, A. Bachmatiuk, V. Bezugly, J. Kunstmann, T. Gemming, Z. Liu, G. Cuniberti, M.H. Rümmeli, Electron-beam induced synthesis of nanostructures: a review, Nanoscale 8 (2016) 11340–11362.
[5] I. Gonzalez-Martinez, A. Bachmatiuk, T. Gemming, B. Trzebicka, Z. Liu, M.H. Rummeli, Rapid synthesis of pristine graphene inside a transmission electron microscope using gold as catalyst, Commun. Chem. 2 (2019) 33.
[6] L. Kai, F. Shen, A novel approach for preparing silver nanoparticles under electron beam irradiation, J. Nanoparticle Res. 12 (2009) 1423–1428.
[7] R. Egerton, Control of radiation damage in the **TEM**, Ultramicroscopy 127 (2013) 100–108.
[8] R. Egerton, Mechanisms of radiation damage in beam-sensitive specimens, for **TEM** accelerating voltages between 10 and 300 kV, Microscopy Res. Tech. 75 (2012) 1550–1556.
[9] Q. Ru, Nanocrystals synthesized by electron-beam induced fragmentation of vacancy-containing metals microspheres, Appl. Phys. Lett. 71 (13) (1997) 1792–1794.
[10] P.D. Angel, J. Rodriguez-Hernandez, A. García-Bórquez, J.M. de la Fuente, Nucleation and growth of **NiO** nanoparticles and thin films by **TEM** electron irradiation, Catal. Today 212 (2013) 194–200.
[11] Z. Pan, Z. Dai, Z. Wang, Lead oxide nanobelts and phase transformation induced by electron beam irradiation, Appl. Phys. Lett. 80 (2) (2002) 309–311.
[12] P. Herley, W. Jones, The generation of nanoscale metal particles from metal azides: A high resolution electron microscopic study, Z. Phys. D Atoms Molecules Clusters 26 (1) (1993) 159–161.
[13] W.D. Pyrz, P. Sangmoon, T. Vogt, D.J. Buttrey, Electron beam-induced fragmentation and dispersion of **Bi-Ni** nanoparticles, J. Phys. Chem. C 111 (29) (2007) 10824–10828.
[14] M. Buck, I. Sines, R. Schaak, Liquid-phase synthesis of uniform cube-shaped **GeTe** microcrystals, Chem. Mater. 22 (10) (2010) 3236–3240.
[15] K. Wang, H. Wu, W. Yuan, W. Xi, J. Luo, Simple physical preparation of single copper atoms on amorphous carbon via Coulomb explosion, Nanoscale 11 (2019) 7595–7599.
[16] P. Wang, Y. Zhao, G. Wang, T. Lu, Novel growth mechanism of single crystalline **Cu** nanorods by electron beam irradiation, Nanotechnology 15 (1) (2003) 218.
[17] N. Jiang, Electron irradiation effects in transmission electron microscopy: Random displacements and collective migrations, Micron 171 (2023) 103482.
[18] I. Gonzalez-Martinez, K. Weinel, W. Feng, L. Agudo Jacome, T. Gemming, B. Büchner, Hybrid tungsten-carbon 2**D** nanostructures via in-situ gasification of carbon substrates driven by ebeam irradiation of $\mathbf{WO}_{2.9}$ microparticles, Nanotechnology (2023).
[19] J. Zhang, L. Zhu, Y. Yang, H. Yong, J. Zhang, Y. Peng, J. Fu, A Coulomb explosion strategy to tailor the nano-architecture of α-$\mathbf{MoO}_3$ nanobelts and an insight into its intrinsic mechanism, Nanoscale 10 (2018) 8285–8291.
[20] Y. Chen, Y. Huang, N. Liu, J. Su, L. Li, Y. Gao, Fabrication of nanoscale **Ga** balls via a Coulomb explosion of microscale silica-covered **Ga** balls by **TEM** electron-beam irradiation, Sci. Rep. 5 (1) (2015) 1–7.
[21] I. Gonzalez-Martinez, S.M. Gorantla, A. Bachmatiuk, V. Bezugly, J. Zhao, T. Gemming, J. Kunstmann, J. Eckert, G. Cuniberti, M.H. Rümmeli, Room temperature in situ growth of $\mathbf{B}/\mathbf{BO}_x$ nanowires and $\mathbf{BO}_x$ nanotubes, Nano Lett. 14 (2) (2014) 799–805.
[22] I. Gonzalez-Martinez, T. Gemming, R. Mendes, A. Bachmatiuk, V. Bezugly, J. Kunstmann, J. Eckert, G. Cuniberti, M.H. Rümmeli, In-situ quasi-instantaneous e-beam driven catalyst-free formation of crystalline aluminum borate nanowires, Sci. Rep. 6 (1) (2016) 1–9.
[23] N. Jiang, On the in situ study of **Li** ion transport in transmission electron microscope, J. Mater. Res. 30 (2015) 424–428.
[24] N. Jiang, The mechanism of nanoparticle precipitation induced by electron irradiation in transmission electron microscopy, Ultramicroscopy 196 (2019) 18–23.
[25] R. Egerton, Radiation damage to organic and inorganic specimens in the **TEM**, Micron 119 (2019) 72–87.
[26] F. Solá, O. Resto, A. Biaggi-Labiosa, L.F. Fonseca, Electron beam induced growth of silica nanorods and heterostructures in porous silicon, Nanotechnology 18 (40) (2007) 405308.
[27] E. Longo, L.S. Cavalcante, D.P. Volanti, A.F. Gouveia, V.M. Longo, J.A. Varela, M.O. Orlandi, J. Andrés, Direct in situ observation of the electron-driven synthesis of **Ag** filaments on α-$\mathbf{Ag}_2\mathbf{WO}_4$ crystals, Sci. Rep. 3 (2013) 1676.
[28] W.L. Bragg, XIII. The crystalline structure of copper, Lond. Edinb. Dublin Philos. Mag. J. Sci. 28 (165) (1914) 355–360.
[29] H. Chessin, W.C. Hamilton, B. Post, Position and thermal parameters of oxygen atoms in calcite, Acta Crystallograph. 18 (4) (1965) 689–693.
[30] M.A. Hubbe, C. Maitland, M. Nanjiba, T. Horst, K. Ahn, A. Potthast, Archival performance of paper as affected by chemical components: A review, BioResources 18 (3) (2023) 6430–6498.
[31] R. Schlögl, H. Boehm, Influence of crystalline perfection and surface species on the X-ray photoelectron spectra of natural and synthetic graphites, Carbon 21 (4) (1983) 345–358.
[32] M. Shiraishi, M. Inagaki, X-ray diffraction methods to study crystallite size and lattice constants of carbon materials, Carbon Alloys: Novel Concepts Dev. Carbon Sci. Technol. (2003) 161–173.
[33] J. Cazaux, Correlations between ionization radiation damage and charging effects in transmission electron microscopy, Ultramicroscopy 60 (3) (1995) 411–425.
[34] M. Berger, J. Coursey, M. Zucker, **ESTAR**, **PSTAR**, and **ASTAR**: Computer programs for calculating stopping-power and range tables for electrons, protons, and helium ions (version 1.21), 1999.
[35] K. Kanaya, H. Kawakatsu, Secondary electron emission due to primary and backscattered electrons, J. Phys. D: Appl. Phys. 5 (9) (1972) 1727.
[36] K. Kanaya, S. Ono, F. Ishigaki, Secondary electron emission from insulators, J. Phys. D: Appl. Phys. 11 (17) (1978) 2425.
[37] S. Ono, K. Kanaya, The energy dependence of secondary emission based on the range-energy retardation power formula, J. Phys. D: Appl. Phys. 12 (4) (1979) 619.
[38] T. Kiuru, J. Mallat, A.V. Räisänen, T. Närhi, Schottky diode series resistance and thermal resistance extraction from **S**-parameter and temperature controlled **IV** measurements, IEEE Trans. Microw. Theory Tech. 59 (8) (2011) 2108–2116.
[39] R.U.R. Sagar, X. Zhang, J. Wang, C. Xiong, Negative magnetoresistance in undoped semiconducting amorphous carbon films, J. Appl. Phys. 115 (2014) 123708.
[40] A.S. Saleemi, R. Singh, Z. Luo, X. Zhang, Structure dependent negative magnetoresistance of amorphous carbon thin films, Diam. Relat. Mater. 72 (2017) 108–113.
[41] Y. Hishiyama, H. Irumano, Y. Kaburagi, Y. Soneda, Structure, Raman scattering, and transport properties of boron-doped graphite, Phys. Rev. B 63 (2001) 245406.

[42] O. Txoperena, Y. Song, L. Qing, M. Gobbi, L.E. Hueso, H. Dery, F. Casanova, Impurity-assisted tunneling magnetoresistance under a weak magnetic field, Phys. Rev. Lett. 113 (2014) 146601.
[43] H. Zhou, Y. Zhang, W. Zhao, Tunable tunneling magnetoresistance in van der waals magnetic tunnel junctions with 1**T**-**CrTe**$_2$ electrodes, ACS Appl. Mater. Interfaces 13 (1) (2021) 1214–1221.
[44] W. Zhu, Y. Zhu, T. Zhou, X. Zhang, H. Lin, Q. Cui, F. Yan, Z. Wang, Y. Deng, H. Yang, L. Zhao, I. Žutić, K.D. Belashchenko, K. Wang, Large and tunable magnetoresistance in van der waals ferromagnet/semiconductor junctions, Nature Commun. 14 (2023).
[45] T. Song, X. Cai, M.W.-Y. Tu, X. Zhang, B. Huang, N.P. Wilson, K.L. Seyler, L. Zhu, T. Taniguchi, K. Watanabe, M.A. McGuire, D.H. Cobde, D. Xiao, W. Yao, X. Xu, Giant tunneling magnetoresistance in spin-filter van der waals heterostructures, Science 15 (6394) (2018) 1214–1218.
[46] X. Zhang, Q. Xue, D. Zhu, Positive and negative linear magnetoresistance of graphite, Phys. Lett. A 320 (2004) 471–477.